IMAGES OF GRADUAL MILLIMETER EMISSION AND MULTI–WAVELENGTH OBSERVATIONS OF THE 1994 AUGUST 17 SOLAR FLARE

Adriana V. R. Silva*
Solar Astronomy 264-33, Caltech, Pasadena, CA 91125

R. P. Lin
Physics Department and Space Sciences Laboratory, University of California, Berkeley, CA 94720

Imke de Pater
Astronomy Department, University of California, Berkeley,CA 94720

Stephen M. White
Dept. of Astronomy, University of Maryland, College Park, MD 20742

K. Shibasaki and H. Nakajima
Nobeyama Radio Observatory, Minamisaku, Nagano 384-13, Japan

Abstract. We present a comprehensive analysis of the 1994 August 17 flare, the first flare imaged at millimeter (86 GHz) wavelengths. The temporal evolution of this flare displays a prominent impulsive peak shortly after 0102 UT, observed in hard X–rays and at microwave frequencies, followed by a gradual decay phase. The gradual phase was also detected at 86 GHz. Soft X–ray images show a compact emitting region ($\lesssim 20''$), which is resolved into two sources: a footpoint and a loop top source. Nonthermal emissions at microwave and hard X–ray wavelengths are analyzed and the accelerated electron spectrum is calculated. This energy spectrum derived from the microwave and hard X–ray observations suggests that these emissions were created by the same electron population. The millimeter emission during the gradual phase is thermal bremsstrahlung originating mostly from the top of the flaring loop. The soft X–rays and the millimeter flux density from the footpoint source are only consistent with the presence of a multi–temperature plasma at the footpoint.

Key words: Sun: flares; Sun: radio radiation; Sun: X–rays

1. Introduction

With the advent of multi–element millimeter arrays, it has become possible to image solar flares, which allows the determination of the brightness temperature, total flux density, and optical depth of millimeter sources. When multiple sources are present, their individual characteristics can only be discerned by mapping the sources. Precise positional

* also Physics Dept., New Jersey Institute of Technology, Newark, NJ 07102

information on the millimeter sources is needed to see whether there is spatial coincidence with simultaneous sources at other wavelengths. Comparison with emission at other wavelengths is necessary in order to determine the millimeter emission mechanism. The nonthermal millimeter emission, generally produced in the impulsive phase of flares, is believed to be gyrosynchrotron radiation produced by electrons with energies of approximately 1 MeV (Ramaty 1969, Ramaty & Petrosian 1972, White & Kundu 1992). On the other hand, the microwaves are thought to originate from gyrosynchrotron radiation from a few hundred keV electrons, whereas the $<$50 keV hard X–rays by $<$100 keV electrons. Thus, simultaneous hard X–ray, microwave, and millimeter observations may be used to probe the accelerated electron spectrum over a broad range of energies. Conversely, the thermal millimeter emission is thought to be free–free emission from the post–flare loops filled with hot plasma. Since these hot loops are seen in soft X–rays, the millimeter and soft X–ray observations should be analyzed jointly.

Previous millimeter observations were carried out using single dishes (Kaufmann et al. 1984, 1985, Herrmann 1992) or interferometers with few antennas. Nakajima et al. (1985) used a two antenna interferometer for solar observing at Nobeyama achieving 10 sfu sensitivity at 80 GHz. Kundu et al. (1990) report the first high sensitivity (0.02 sfu) interferometric observations using the Berkeley-Illinois-Maryland Array (BIMA, Welch et al. 1996), a millimeter interferometer with three antennas at the time. Such a small number of antennas, however, is not enough to make snapshot (less than a minute) images of the flaring region, while fast mapping is necessary to follow the rapid evolution of flares. The lack of knowledge of the millimeter source location makes it difficult to associate the millimeter emission with sources at other wavelengths (Silva et al. 1996b). This is particularly problematic in flares with multiple sources (the vast majority of flares). In the summer of 1994, BIMA resumed operations after being upgraded to six antennas, and currently it consists of 9 antennas.

The first millimeter images of a solar flare obtained with the upgraded BIMA are analyzed here. A subset of the data was reported by Silva et al. (1996a). Unfortunately, BIMA was on a calibration scan during the impulsive peak, thus the interferometer only observed the gradual phase of the flare. In the following section we discuss the observations: the pre–flare configuration of magnetic loops seen in soft X–rays; a brief overview of the evolution of the flare; the physical parameters of the millimeter source; and the soft (continuum and line) and hard X–ray observations. Section 3 discusses the microwave and the hard X–ray spectra, which provide information on the nonthermal electron population, and the comparison of the millimeter emission and the soft

X–rays from the hot emitting plasma in order to determine the 3.3 mm emission mechanism. The last section lists the conclusions.

2. Observations

The M1.5 flare (GOES flux of 1.5×10^{-2} erg/cm^2 s) observed on 17 August 1994 occurred shortly after 0100 UT. The flare heliocentric position was at S15 W35 in active region AR7765. This burst was simultaneously detected by BIMA at 86 GHz, by the Nobeyama Radio Observatory (NRO) interferometer at 17 GHz and in total power at 2.0, 3.75 and 9.4 GHz; in X–rays by the Soft (SXT, Tsuneta et al. 1991) and Hard (HXT, Kosugi et al. 1991) X–ray Telescopes, and by the Bragg Crystal Spectrometer (BCS, Culhane et al. 1991) on board *Yohkoh*. The microwave observations were taken with the single radiometers at Nobeyama: 2.0 GHz (2 m dish), 3.75 GHz (1.5 m dish), and 9.4 GHz (80 cm dish), whereas the 17 GHz emission was observed with the eighty–four 80 cm antennas also at Nobeyama. The millimeter data were taken with four dishes at BIMA (Welch et al. 1996), spread out on an inverted T configuration, allowing crude mapping of the millimeter emission.

2.1. Pre–flare configuration

A movie of soft X–ray images of AR 7765 prior to the flare shows as its brightest feature a stable compact ($\sim$10″) loop (labeled 'old' in Figure 1). This loop is seen to expand slowly outward. Figure 1 shows an SXT pre–flare image of the region, four minutes before the impulsive peak of the flare. At this time, the activation of a new compact loop (labeled 'new'), nested within the old one, is observed. This new loop is where the flare occurred.

Figure 2 shows an overlay of the flare soft X–ray image (gray scale) taken during the gradual phase onto a magnetogram from Kitt Peak (made 10 hours prior to the flare). Positive polarity magnetic fields are shown as solid contours, while the broken line contours represent negative polarity fields. This overlay shows that the flare loop connects the penumbra of a positive sunspot (maximum field of 500 Gauss) to an island of weak negative polarity just to the west of it. The soft X–ray source is probably located at the top of the loop, since it overlies a magnetic neutral line. The southern footpoint is anchored in a region of positive polarity, whereas the other footpoint, not seen in soft X–rays, is thought to be located at a region of negative polarity approximately 20″ to the North.

2.2. Evolution of the flare

Figure 3 shows the time profiles of the flare emission at different wavelengths. As can be seen from the figure, the temporal evolution of the flare consists basically of an impulsive peak at ∼0102:15 UT, which lasted for ∼15 seconds, and a gradual phase with a maximum at 0112-0113 UT that lasted for approximately 20 minutes. The top panel presents the soft X–ray emission from SXT (asterisks), and the hard X–rays from the two lower energy channels of HXT: 14-23 keV (LO) and 23-33 keV (M1) channels. There was hardly any emission above 33 keV. The hard X–ray emission shows a small impulsive peak at ∼0102 UT, and two broad peaks at 0105 and 0109 UT. Since flare mode was triggered just after the maximum of the impulsive HXT peak, there is no recorded emission in the HXT M1–channel prior to the trigger. Nevertheless, the impulsive peak at ∼0102 UT is the strongest feature seen in the M1–channel count rates. By 0113 UT all the hard X–ray emission has ceased. The soft X–rays produced by the flare started its rise at around 0102 UT, reached maximum values around 0111 UT, and lasted for about 15 minutes.

The two bottom panels of Figure 3 show the radio emission from 2 to 86 GHz. The impulsive peak at 0102:15 UT is very strong at microwave frequencies. The impulsive phase lasted approximately 15 seconds, reaching 4, 11.5, 28, and 27 sfu at 2.0, 3.75, 9.4 and 17 GHz, respectively. Unfortunately, BIMA was on a calibration scan during this impulsive peak, which prevented detection of the flare at 86 GHz. Curiously, the impulsive phase, with such strong signature at 4-17 GHz, produced a relatively small peak in the HXT LO–channel. The LO–channel peak around 0102 UT is ∼2.5 times smaller than the broad peak three minutes later. This same impulsive peak, however, is the main feature in the M1–channel. The gradual phase that followed had a maximum of 18 sfu at 17 GHz around 0110-1015 UT, and lasted for 30 minutes. The 86 GHz and the other microwave emissions seem to follow the gradual 17 GHz time profile. The millimeter emission has a broad peak at 0111-0115 UT, and lasts until 0140 UT.

The intrinsic time resolution of the millimeter data is 2 seconds. Since there was no spatial evolution observed in the millimeter source, the maps were integrated over 2 minutes to increase their (u,v) coverage, and hence decrease the mapping ambiguities. The calibration and mapping of the 86 GHz observations were done using the BIMA data reduction and analysis software package MIRIAD (Wright & Sault 1993).

Figure 4 shows how the millimeter source relates spatially to the sources at other wavelengths, at four different times (rows) throughout the flare. The columns correspond to maps of SXT (first two columns), HXT LO, HXT M1, NRO (17 GHz), and BIMA (86 GHz), from left to right respectively. Pre–flare images of the flare are displayed on the top row (SXT and NRO only). The soft X–ray image at this time shows multiple loops, and the flare site (marked by the dashed cross hairs) is already bright. The same overall structure envelope is outlined in the pre–flare 17 GHz map. During the flare, a compact emitting region ($< 20''$) is seen in X–ray maps. The first column shows a blow–up of the soft X–ray flaring loop, which is seen to consist of two sources. Early in the flare, the southern source dominates the emission, whereas later on, most of the soft X–rays originates from the northern source. The LO–channel hard X–ray maps are 10 seconds integration, while the M1 maps needed 50 seconds integration due to the low counts in this channel. The source seen in hard X–ray maps is basically unresolved.

The millimeter maps shown in the last column of Figure 4 show a slightly resolved single source. The very elongated shape of the source is a consequence of the fairly elongated synthesized beam ($60''\times 6''$), plotted on the upper right corner, because the flare occurred almost at sunset in California.

2.3. Physical parameters of the millimeter source

By modeling the visibilities of the 86 GHz data, the source size, total flux density, and brightness temperature of the source seen in the BIMA maps are calculated. The millimeter source was assumed to be a circular Gaussian source (the simplest model of an extended source). The physical parameters obtained from the fit as a function of time are shown in Figure 5. The total flux density from the millimeter source as function of time (Figure 5a, diamonds) agrees well with the flux density measured in the shortest baseline (dashed line on all four panels), as it should. The total flux density reaches a maximum of 9 sfu at approximately 0111 UT. The source diameter at half-power (Figure 5b) is $7''$ on average during the peak of the gradual phase. Since the changes in source radius are within the error of measurements, the source size may be considered constant throughout the flare.

The brightness temperature, T_b, of the source is determined from the total flux density and source size using the Rayleigh–Jeans approximation to Planck's law. Because the source size remains basically constant, the time evolution of T_b is the same as that of the flux density. The peak brightness temperature, T_b, corresponding to the pixel of maximum flux density of the millimeter source reaches a maximum of 1.2×10^6 K at 0111 UT.

The optical depth can be estimated if the physical temperature of radiating electrons, T_e, is known, since $T_b = T_e(1 - e^{-\tau})$. The electron temperature as a function of time is obtained from the soft X–ray data (Figure 6a, discussed below) through SXT filter ratios (Vaiana et al. 1973, Gerassimenko & Nolte 1978, Hara et al. 1992, McTiernan et al. 1993). The resulting optical depth as a function of time is plotted on Figure 5c, and has the same time profile as the millimeter flux density (dashed line). Its maximum value is 0.09, thus, confirming that the millimeter emission is indeed optically thin, as expected.

2.4. X–ray observations

The soft X–ray images from SXT show two sources: a compact source early in the flare, and a source with a more gradual time profile which dominates the emission at later times. The boxes in the first column of Figure 4 outline the two distinct sources. The early source (the southern one) is located at the penumbra of a positive polarity sunspot (shown in Figure 2); it is therefore identified as a footpoint source. The other source is thought to be at the top of the magnetic loop since it overlies a magnetic neutral line.

Light curves of both the footpoint and loop top sources were obtained by totaling the flux within the boxes outlined in Figure 4. The light curve of the footpoint source peaks at 0105 UT, and its time evolution follows that of the HXT LO–channel, which also displays a maximum at this time. In contrast, the soft X–ray flux from the loop top source displays a broad maximum from 0110-0113 UT. Temperature and emission measure ($\mathcal{EM}$) maps were calculated for each pixel in the SXT images by taking filter ratios. The time evolution of the temperature and $\mathcal{EM}$ for both sources (within the boxes in Figure 4) are shown in Figure 6. The temperature of the footpoint source remains basically constant over time at 10 MK, while emission from the loop top source displays a 12–13 MK peak at 0112-0115 UT (Figures 6a, asterisks and crosses, respectively). The time evolution of the emission measure (Figures 6b) is quite distinct between the loop top and footpoint source, with the former reaching peak values $\sim$ 7 minutes later and almost 3 times higher than the footpoint source. The average ion density of each source, $n_i = \sqrt{\mathcal{EM}/V}$ (where V is the volume of the source), is $\sim 4 - 4.5 \times 10^{11}$ cm^{-3} at maximum for both sources.

The BCS soft X–ray line data were analyzed in search of blue–shifts, which would suggest evaporating plasmas. We found no significant blue–shifts: the maximum calculated up–flows from Ca XIX was $\sim$70 km/s at 0103:30 UT. The Fe XXV data was fit by a single stationary component of temperature $\sim$18-22 MK (Figure 6a). The temperature and emission measure of the hot soft X–ray source obtained from the line fitting are shown in Figure 6a and b as triangles.

Since the time profile of the Fe XXV emission is remarkably similar to the HXT LO–channel light curve, it is likely that the HXT LO count rates have a substantial contribution of thermal emission. The thermal contribution from this hot source to the HXT emission was calculated and amounts to half of the photons detected in the LO channel, while the contribution to the M1 channel was negligible. The thermal contribution of the hot Fe XXV source was subtracted from the HXT channels before the hard X–ray spectrum was constructed for the study of the nonthermal component (see Section 3.2).

3. Results and Discussion

In order to define the physical parameters of the microwave emission, we separate the microwave radiation into its thermal and nonthermal components. Then, the radio spectrum of each component is independently fit by either thermal bremsstrahlung or nonthermal gyrosynchrotron radiation. Once the distribution of energetic electrons that produced the microwave emission is determined from its spectrum, this electron population is compared with the electrons that generated the hard X–rays. The last part of this section studies the emission at millimeter wavelengths during the gradual phase and how it compares with the soft X–ray emission.

3.1. Microwave spectra

Before the spectra can be constructed, the nonthermal and thermal contributions need to be determined. Thus, we modeled the thermal emission and then subtracted it from the total microwave flux densities, obtaining the nonthermal component. The thermal contribution is modeled as follows. Prior to 0110 UT, the temporal evolution of the thermal component was taken from the light curve of GOES soft X–rays, since this emission is likely to be solely due to thermal emission. Soft X–rays from GOES were chosen instead of *Yohkoh* because the Nobeyama data is the integral flux from the entire solar disk. After 0110 UT, the radio emission is probably completely thermal, thus we used the same microwave flux averaged over one minute as the thermal model. The microwave light curves and their respective thermal components (dashed lines) are shown in Figure 7 (left column). The right column depicts the resultant nonthermal components at 2.0, 3.75, 9.4, and 17.0 GHz after the thermal model has been subtracted.

The radio spectra of the flare were constructed using total–power flux densities at 2.0, 3.75, 9.4, and 17 GHz. We have excluded the 86 GHz flux density because it is obtained from interferometric data which 'resolve out' large scale structures. The thermal and nonthermal spectra were analyzed separately. The spectra constructed from the thermal component was fit by free–free emission according to eq. (20) of Dulk (1985). The nonthermal component was fitted by nonthermal gyrosynchrotron radiation from electrons with power–law distribution in energy (eqs. [35] and [36] of Dulk 1985).

Nonthermal gyrosynchrotron emission is a function of the magnetic field, the angle between the magnetic field and the line–of–sight, the total number of energetic electrons, the power–law index of electron energy distribution, and the source size. In order to reduce the number of free parameters, we adopted a constant magnetic filed strength of 350 Gauss (compatible with photospheric magnetogram), and a constant angle of 50^o. Examples of the gyrosynchrotron fit to the nonthermal component of the microwave spectra are shown as dotted lines on Figure 8. The parameters obtained from these fits, namely the power–law index, δ_r, the total number of electrons, $N_e(E > E_0)$, and the source size, d_{nt}, are listed in Table I. Since the radio nonthermal emission ceases at ~0105 UT, only the spectrum at the time of peak radio emission (Figure 8a) and at 0103:45 UT (Figure 8b) show gyrosynchrotron spectra.

The power–law index is very hard at the time of the peak, $\delta_r \sim 2$, and steepens later on to $\delta_r \sim 4$. Assuming thick target case, the power–law index of the energy distribution of the electrons which produced the observed hard X–ray spectrum is $\delta_x = 2.6$ at 0102 UT and 3.7 at 0104 UT. These values are not too different from those inferred from the radio spectra. The fitted source size of $\sim 6''$ is small, however we would like to point out that this is a very compact loop, whose hard X–ray source is unresolved (size $<5''$).

As mentioned above, the radio thermal component was fit as thermal bremsstrahlung, which depends on the temperature, emission measure, and size of the source. The source size used was the average of the minor and major axis measured from the source in the 17 GHz maps (Figure 4). The two remaining parameters, namely the temperature and emission measure, are listed in Table I. The fits to the radio thermal component are shown as dashed lines in Figure 8.

Figure 8a displays the radio spectrum (asterisks) during the impulsive peak prior to any thermal emission, hence the emission is purely nonthermal, and the gyrosynchrotron model is shown as a dotted line. Figure 8b shows the radio spectrum during a period when both thermal and nonthermal emissions are important. Both thermal (triangles) and nonthermal (crosses) components were fit independently by free–free (dashed line) and gyrosynchrotron (dotted line) radiation, respectively. The sum of both models is shown as a solid line, where the asterisks represent the observed total flux density (thermal plus nonthermal). The last two panels of Figure 8 depict the radio spectrum during the gradual phase of the flare and long after all the nonthermal emission has ceased. The free–free fit to the microwave data based on the parameters listed in Table I are shown as dashed lines. For comparison, we have also plotted as a dot-dash line the free–free flux from the soft X–ray emitting plasma detected by GOES. This flux density was calculated using the temperature and emission measure inferred from the GOES data and an assumed source size of $20''$ (approximately the size of the soft X–ray source seen in SXT maps). It is clear from Figures 8c and d that the hot (8-12 MK) plasma seen in soft X–ray is not enough to account for the microwave emission. Rather, the radio emission seem to be mostly due to a cooler ($\sim$6 MK) and extended ($\sim 40''$) plasma. The emission at 86 GHz is not expected to follow the microwave spectrum since the BIMA interferometer resolves flux from sources larger than $20''$.

Note that the 2.0 GHz flux density is consistently larger than the flux inferred from the models. This may suggest the existence of yet another radio source, cooler and more extended than the one characterized by the models.

3.2. Accelerated electron energy distribution

Electrons in the 20-100 keV energy range are assumed to produce the observed hard X–rays, while the microwave emission is thought to originate from $\gtrsim$ 300 keV electrons. The energy spectrum of the electrons which produced the hard X–ray and microwave emission is determined from the spectra calculated separately from each data set. Figure 9 shows the electron energy distribution constructed from the hard X–ray (dashed line), assuming thick target, and radio (solid line) spectra at $\sim$0102 UT (the time of the impulsive peak) and at $\sim$0104 UT. Both electron spectra assumed a lower energy cutoff of 10 keV. The spectrum at the time of the peak (Figure 9, top) flattens slightly from $\delta_x \sim 2.6$ to $\delta_r \sim 2.0$, while the opposite occurs at $\sim$0104 UT with the spectrum breaking somewhat down from $\delta_x \sim 3.7$ to $\delta_r \sim 4.2$. However, the difference in spectral slope from <100 keV to >300 keV electrons is only $\sim$0.5. Since this difference is within the uncertainty in the spectral fitting of hard X–rays and microwaves, we consider the emission at both wavelengths to have been produced by the same population of accelerated electrons. As can be seen from Figure 9, the electron energy spectrum was hardest at the peak of hard X–ray emission ($\delta \sim 2-2.5$), becoming steeper ($\delta \sim 4$) later on at 0104 UT. This is the so called soft–hard–soft behavior of the hard X–ray spectral index observed in other flares.

3.3. Radio emission from the soft X–ray emitting plasma

In order to determine if the 86 GHz emission is thermal, we compare it to the inferred free–free emission from the hot plasma seen by SXT. The free–free radio flux density is calculated from the emission measure and temperature determined from the soft X–ray emitting plasma. The optically thin ($\tau \ll 1$) free–free flux density is given by (Dulk 1985)

$$S_{free} \simeq 1.12 \times 10^6 \, \frac{\mathcal{EM}_{55}}{\sqrt{T_6}} \, (17.59 + \ln T_6 - \ln \nu_{GHz}) \quad \text{sfu} \quad (\tau \ll 1), \qquad (1)$$

where ν_{GHz} is the frequency in GHz, $\mathcal{EM}_{55}$ is the emission measure in units of 10^{55} cm^{-3}, and T_6 is the temperature in millions of degrees. Using the temperature and emission measure, $\mathcal{EM}$, calculated from SXT maps for the individual sources, we constructed maps of the radio emission. Since $S_{free} \propto \mathcal{EM}$, the morphology of these maps is very similar to the SXT brightness maps (Figure 4).

The total, spatially integrated, radio flux density predicted at 86 GHz based upon an isothermal soft X–ray model from SXT observations is plotted in Figure 10a (triangles). BIMA being an interferometer, however, will 'resolve out' flux from extended ($\gtrsim 20''$) features. In order to determine BIMA's response to this "radio source", we folded the SXT predicted radio maps through the BIMA instrument response. The result, the total flux density which should be seen by BIMA, is plotted on Figure 10a as diamonds. Since the flux density predicted for BIMA (diamonds) is less than the total, spatially integrated, radio flux density contained in the radio maps generated from SXT data (triangles), BIMA indeed 'resolves out' some of the flux from the extended structures seen in the SXT maps. The observed flux density at 86 GHz is plotted as a solid line on Figure 10. Due to the uncertainty in the attenuation used to keep the strong solar signal from saturating the system, the absolute calibration for BIMA solar data for these observations was uncertain to within 50%. We adopted the maximum value for the attenuation, thus BIMA's absolute flux density ranges from the value plotted in Figure 5a to half this value. Note, that the agreement between the expected and observed flux densities (diamonds and solid line) is very good for times later than 0120 UT, thus validating our choice for the attenuation value. The resolved SXT predicted radio flux density (diamonds), however, is higher than the observed BIMA flux density (solid line), especially during the rise of the millimeter flux density, by about $\gtrsim 40\%$.

The free-free radio flux densities of the footpoint (asterisks) and the loop top (crosses) SXT sources (first column of Figure 4) were calculated using eq. (1) and are plotted on Figure 10a. The agreement between the observed millimeter emission and the predicted free–free flux density at 86 GHz from the soft X–ray emitting plasma at the top of the magnetic loop is excellent.

Since the SXT footpoint source appeared not to have been detected by BIMA, we first tried modeling the soft X–ray emission from the footpoint source as nonthermal. The nonthermal gyrosynchrotron flux density at 86 GHz would be much less than the thermal flux density from the loop top source, due to the low magnetic field strength ($\lesssim 400$ Gauss) at the flare site. Such a small flux density is not expected to be observed. In order to investigate further a possible nonthermal origin of the soft X–rays, we modeled the X–ray emission (SXT and HXT) as being generated by an instantaneous electron population with a double power–law energy distribution. The instantaneous electrons, with energy below a certain break energy, E_b, were chosen to follow a power–law spectrum with a slope $\delta_s = 1.5$, in order to fit the SXT spectrum, whereas the electrons with energy above E_b had a power–law index, δ_h, determined from the HXT count rates spectra after subtraction of the contribution from the hot Fe XXV source. At 0102:30 UT, $\delta_h \sim 2.5$, it gradually increases to 4 at 0105 UT, and remains constant at $\sim$5-6 through the end of HXT flux at 0112 UT.

The ion density of the footpoint source was assumed to be constant over time $n_i = 10^{11}$ cm^{-3}. The volume was kept fixed at $V = 3.6 \times 10^{26}$ cm^3 (source size of $10''$). The bremsstrahlung cross–section used is given by the Bethe-Heitler formula (Koch and Motz 1959) with the Elwert correction factor (Elwert & Haug 1969). The only free parameter in the model was the break energy, E_b. We adopted an instantaneous electron flux (with δ_s, δ_h and E_b) from 1 keV to 100 keV, from which the photon flux was derived following Brown (1971) and Lin (1974). The calculated photon flux was then compared to the observations: the nonthermal photon flux from the SXT footpoint source and the HXT count rates spectrum. The break energy was varied until the agreement of the model with the data was satisfactory. This fit was repeated for different times throughout the flare. An example of the modeled electron density spectrum and the corresponding photon flux spectrum is shown in Figure 11. The data points are plotted as triangles on the photon spectrum. The values of the energy break obtained through the fit explained above are $E_b \sim 3$ keV at 0105 UT, increasing to 7 keV by 0107, and remaining between 6.5 and 8 keV until 0112 UT.

Despite the good agreement between the modeled photon flux spectrum and the observed one, a serious problem resides in the amount of energy contained in such a high number of electrons at low energies (1-2 keV). The input energy rate of the nonthermal electrons at the loop footpoint varies from $2-8\times 10^{31}$ erg/s, resulting in a total of $\sim 6\times 10^{32}$ erg injected during a period of 9 minutes. Most of this energy is contained in the 1-2 keV electrons. The maximum instantaneous thermal energy from the region, estimated from SXT data, is $\sim 2\times 10^{30}$ erg. The total injected energy at the footpoint is 300 times larger than the instantaneous thermal energy. Such large energy input would heat large quantities of plasma to high temperatures, which would subsequently produce a much larger soft X–ray flux than is observed. Therefore, the soft X–rays from the footpoint source cannot be attributed to a nonthermal source, since in that case, a much larger soft X–ray flux due to heating should have been observed. This is the same criticism (Hudson et al. 1994) made to a nonthermal origin of soft X–rays.

Usually it is assumed that the soft X–ray sources are isothermal, however, a more realistic model may involve multi–temperature sources. We propose that the footpoint source to consist of two components: a hot source and a cold source. The Fe XXV soft X–ray line observations by the Bragg Crystal Spectrometer (BCS) indicate the presence of a $\sim$22 MK source. Since BCS has no spatial information and because the temporal evolution of the Fe XXV source's emission measure seems to follow that of the SXT footpoint source (see Figure 6b), we assume this hot source to be located at the loop footpoint. Thus, the temperature ($\sim$22 MK) and emission measure (1.5×10^{48} cm^{-3}) of the footpoint hot component was obtained from the Fe XXV data. The soft X–ray flux of the footpoint hot component was subtracted from the total flux measured in the various SXT energy bands. The residual flux is assumed to be generated by the cooler component.

The temperature and emission measure which characterize this cooler plasma is assumed to follow the same temporal evolution as the 'old' isothermal footpoint source, and are scaled such that its soft X–ray flux matches the residual flux described above. For scale factors of 0.15 and 1.2 for the 'old' isothermal source's emission measure and temperature (Figure 6a and b, asterisks), respectively, the sum of the flux from the two components agrees within 5-10% with SXT total observed flux from the footpoint source. The resultant temperature and emission measure of the cold footpoint is 12-14 MK and $2-8\times 10^{47}$ cm^{-3}, respectively. The loop top source is assumed to have the same temperature (10-15

MK) and emission measure ($10 - 140 \times 10^{47}$ cm^{-3}) as before (crosses in Figures 6a and b).

The predicted free–free radio flux density for each component of the footpoint source is shown in Figure 10b, as asterisks and triangles for the cold and hot footpoint components, respectively. The total free–free flux density from the multi–temperature footpoint plus loop top (crosses) sources is plotted as diamonds. The figure shows that the predicted flux density from the footpoint source is less than 2 sfu, and the difference between the predicted (diamonds) and observed millimeter (solid line) flux densities is less than $\sim$20%.

4. Conclusions

The 17 August 1994 flare observations presented us with the unique opportunity to image a flare simultaneously at millimeter (86 GHz), microwave (17 GHz), soft and hard X–ray wavelengths. The observations showed both an impulsive phase, with a prominent peak at $\sim$0102 UT in microwaves, followed by a gradual decay phase seen in radio and soft X–ray wavelengths. Soft X–ray images, which have the best spatial resolution ($2\farcs5$), showed the compact ($<20''$) flaring region to consist of two sources: one located at the footpoint and the other at the top of the flaring loop.

The microwave spectrum has been modeled by a combination of thermal and nonthermal components. Gyrosynchrotron fits to the nonthermal microwave spectrum for a magnetic field of 350 Gauss, compatible with the measured photospheric fields of the Kitt Peak magnetograms, yield a nonthermal source size of $\sim 6''$. The spectral index, δ_r of the power–law electrons producing the microwaves was found to be $\delta_r \sim 2$ during the impulsive peak and then increased to 4.2. This power–law index is approximately the same as that calculated from the hard X–rays (thick target case). Since the <50 keV hard X–rays originate from <100 keV electrons, whereas the microwaves are created by electrons of hundreds keV, the agreement in the inferred energy spectrum of the electrons responsible for the microwave emitting electrons are the high energy counterpart of the electrons that produced the hard X–rays. Wang et al. (1994, 1995, 1996) from a joint analysis of microwave and hard X–ray observations of flares also concluded that the emission at both wavelength regimes were due to the same nonthermal electrons.

The free–free radio flux density estimated from the soft X–ray emitting plasma was compared to the millimeter observations. An apparent excess flux density seemed to originate from the footpoint source which was not observed by BIMA. The possibility that the soft X–rays from the footpoint source were nonthermal was ruled out on energy grounds. We conclude that the gradual millimeter emission was optically thin thermal bremsstrahlung coming from a compact source at the top of the magnetic loop (the same source seen in soft X–rays), while the footpoint source consisted of a multi–temperature plasma of hot (22 MK) and cold (12 MK) components. This model matched both the observed soft X–rays and millimeter observations. Since the contribution of this footpoint source to the millimeter flux density is small, most of the emission observed by BIMA is due to the isothermal loop top source.

Acknowledgements

We would like to thank W. J. Welch, the director of BIMA, for allowing a flexible observing schedule (dependent on solar activity). We are grateful to H. S. Hudson for providing the *Yohkoh* data. AVRS acknowledges support by NSF grant AST 93-20238. Solar radiophysics at the University of Maryland is supported by NSF grant ATM 93-16972, by NASA grant NAG W-1541, and NASA/CGRO grant NAG 5-1450. BIMA is supported by NSF grant AST 93-14847.

References

Brown, J. C.: 1971, *Solar Phys.* **18**, 489

Culhane, J. L. et al.: 1991, *Solar Phys.*, **136**, 89

Dulk, G. A.: 1985, *ARA&A* **23**, 169

Elwert, G. & Haug, E.: 1969, *Phys. Rev.* **193**, 90

Gerassimenko, M. & Nolte, J. T.: 1978, *Solar Phys.* **60**, 299

Hara, H., Tsuneta, S., Lemen, J. R., Acton, L. W., & McTiernan, J. M.: 1992, *PASJ*, **44**, L135

Herrmann, R., Magun, A., Costa, J. E. R., Correia, E., & Kaufmann, P.: 1992, *Solar Phys.* **142**, 157

Hudson, H. S., Strong, K. T., Dennis, B. R., Zarro, D., Inda, M., Kosugi, T., & Sakao, T.: 1994, *Astrophys. J.-Letters* **422**, L25

Kaufmann, P., Correia, E., Costa, J. E. R., Dennis, B. R., Hurford, G. J., & Brown, J. C.: 1984, *Solar Phys.* **91**, 359

Kaufmann, P., Correia, E., Costa, J. E. R., Zodi Vaz, A. M., & Dennis, B. R.: 1985, *Nature* **313**, 380

Koch, H. W. & Motz, J. W.: 1959, *Rev. Mod. Phys.* **31**, 920

Kosugi, T., Makishima, K., Murakami, T., Sakao, T., Dotani, T., Inda, M., Kai, K., Masuda, S., Nakajima, H., Ogawara, Y., Sawa, M., & Shibasaki, K.: 1991, *Solar Phys.*, **136**, 17

Kundu, M. R., White, S. M., Gopalswamy, N., Bieging, J. H., & Hurford, G. J.: 1990, *Astrophys. J.-Letters* **358**, L69

Lin, R. P.: 1974, *Space Science Reviews* **16**, 189

McTiernan, J. M., Kane, S.R., Loran, J. M., Lemen, J. R., Acton, L. W., Hara, H., Tsuneta, S., & Kosugi, T.: 1993, *Astrophys. J.-Letters* **416**, L91

Nakajima, H. Sekiguchi, H., Sawa, M., Kai, K., Kawashima, S., Kosugi, T., Shibuya, N., Shinohara, N., & Shiomi, Y.: 1985, *Pub. Astr. Soc. Japan* **36**, 371

Ramaty, R.: 1969, *Astrophys. J.*, **158**, 753

Ramaty, R. & Petrosian, V.: 1972, *Astrophys. J.*, **178**, 241

Silva, A. V. R., White, S. M., Lin, R. P., de Pater, I., Shibasaki, K., Hudson, H. S., & Kundu, M. R.: 1996a, *Astrophys. J.-Letters* **458**, L49

Silva, A. V. R., White, S. M., Lin, R. P., de Pater, I., Gary, D. E., McTiernan, J. M., Hudson, H. S., Doyle, J. G., Hagyard, M. J., Kundu, M. R.: 1996b, *Astrophys. J. Suppl. Ser.* (in press)

Tsuneta, S., Acton, L., Bruner, M., Lemen, J., Brown, W., Carvalho, R., Cortura, R., Freeland, S., Jurcevich, B., Morrison, M., Ogawara, Y., Hirayama, T., & Owens, J.: 1991, *Solar Phys.*, **136**, 37

Vaiana, G. S., Krieger, A. S., & Timothy, A. F.: 1973, *Solar Phys.* **32**, 81

Wang, H., Gary, D. E., Lim, J., & Schwartz, R. A.: 1994, *Astrophys. J.*, **433**, 379.

Wang, H., Gary, D. E., Zirin, H., Nitta, N., Schwartz, R. A., & Kosugi, T.: 1996, *Astrophys. J.*, **456**, 403.

Wang, H., Gary, D. E., Zirin, H., Schwartz, R. A., Sakao, T., Kosugi, T., & Shibata, K.: 1995, *Astrophys. J.*, **453**, 505.

Welch, W. J., Thornton, D. D., Plambeck, R. L., Wright, M. C. M., Lugten, J., Urry, L. Fleming, M., Hoffman, W., et al. 1996, *Publ. Astron. Soc. Pacific*, **108**, 93.

White, S. M. & Kundu, M. R.: 1992, *Solar Phys.* **141**, 347

Wright, M. C. H. & Sault, R. J.: 1993, *Astrophys. J.* **402**, 546

Table I. Parameters used in model spectrum

Time	T_6	$\mathcal{EM}_{49}$	d_{th}	δ_r	$n_e(E > E_0)$	d_{nt}
0102:15				2.0	1.7×10^6	5.6
0103:45	2.5	0.6	36	4.2	1.0×10^9	6.2
0110:50	6.0	2.7	38			
0120:06	6.5	2.3	42			

Figure 1. Pre–flare image from SXT at full resolution ($2\farcs5$) four minutes prior to flare on–set. The two nested magnetic loops discussed in the text are labeled 'new' and 'old'.

Figure 2. Pre–flare magnetogram from Kitt Peak made at 1430 UT of 1994 August 16. Positive and negative polarity magnetic fields are shown as solid and dashed contours, respectively. The positive contours are 0, 50, 100, 200, 300, 400, 500, 600 Gauss, while the negative ones are -20, -50, -100, -200, -300, -400, -500, -600, -700, -800 Gauss. The gray scale represents a SXT flare image at 0107:33 UT.

Figure 3. Time evolution of the different wavelength emissions of the 1994 August 17 flare. The soft and hard X–rays (LO and M1–channel) from SXT and HXT, respectively, are plotted on the top panel. The middle panel shows the time profile of the 17 (NRO) and 86 GHz (BIMA) flux densities, while the bottom panel depicts the radio emission at 2.0, 3.75, and 9.4 GHz (NRO).

Figure 4. Images of the flare at the various wavelengths during four times throughout the flare (rows). The first row shows pre–flare images at 17 GHz and soft X–rays. The maps in each column are from SXT (two left most columns), HXT LO (13-25 keV), HXT M1 (25-35 keV), NRO (17 GHz), and BIMA (86 GHz), from left to right respectively. The first column displays blow–ups of SXT central region. The boxes marked on these panels were the ones used to determine the fluxes from both sources. The hard X–ray sources are unresolved, the contour levels are 20, 50, 70 and 100% of the maximum of each HXT panel.

Figure 5. Temporal evolution of (a) the total flux density, (b) source size, and (c) optical depth obtained from the millimeter maps. The dashed line represents the 86 GHz flux density in BIMA's shortest baseline.

Figure 6. Time evolution of (a) the average temperature and (b) the emission measure of the loop top (crosses) and footpoint (asterisks) sources. These calculations were performed using the soft X–ray flux from the boxes outlined in the previous figure. The triangles represent the temperature and emission measure calculated from the Fe XXV soft X–ray line observations by BCS, using the IDL online fitting procedure.

Figure 7. Left column: Light curves of the total–power Nobeyama emission with the modeled thermal component (dashed line). Right column: Resultant nonthermal component after the thermal model shown in the left column has been subtracted

Figure 8. Plots of microwave spectra at four different times throughout the flare. The nonthermal gyrosynchrotron model is plotted as a dotted line, whereas the thermal bremsstrahlung model is shown as a dashed line. The dot–dash line is the thermal bremsstrahlung obtained from the SXT loop top source. The solid line in (b) is the sum of both gyrosynchrotron and bremsstrahlung emissions. The total observed microwave flux is shown as asterisks, in (b) its thermal and nonthermal components are shown as triangles and crosses, respectively.

Figure 9. Differential energy distribution of energetic electrons calculated from the hard X–ray (dashed line) and microwave (solid line) spectra during the impulsive peak at $\sim$0102 UT and at $\sim$0104 UT.

Figure 10. (a) A plot of the observed millimeter flux density from BIMA (solid line), the calculated free-free flux density from the soft X–ray plasma (triangles), and the BIMA output from the predicted free-free flux density (diamonds). The BIMA output is the flux density that BIMA should have seen from the hot plasma emitting the soft X–rays. Also plotted is the calculated radio flux density at 86 GHz from the isothermal loop top (crosses) and foot point (asterisks) sources. (b) The same as above, only the footpoint source is not isothermal. The footpoint consists of a hot (triangles) and a cold (asterisks) components. The total predicted free–free flux from the multi–temperature footpoint and isothermal loop top sources is shown as diamonds.

Figure 11. The electron energy spectrum (diamonds) calculated for the nonthermal footpoint source at 0105 UT is plotted on the left. The corresponding photon flux spectrum is shown on the right. The data points (SXT footpoint and HXT photon flux) are shown as triangles. For this time the HXT data yield $\delta_x = 5$, a good fit to the observations was obtained for $E_b = 3$ keV.

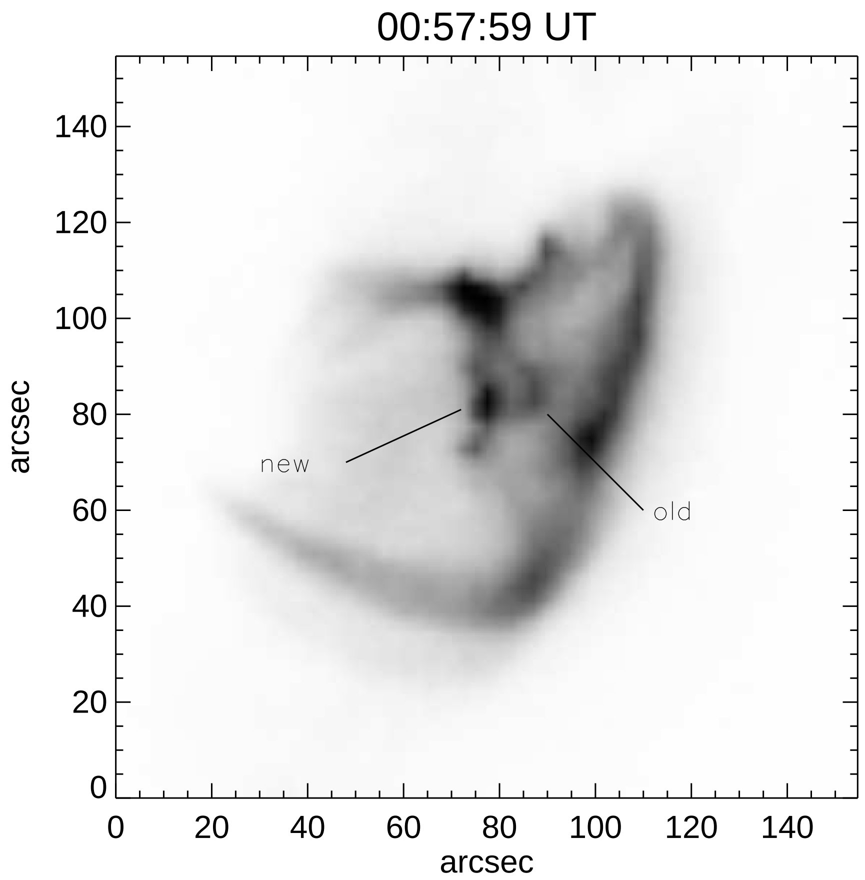

00:57:59 UT
arcsec
arcsec
new
old
0
20
40
60
80
100
120
140

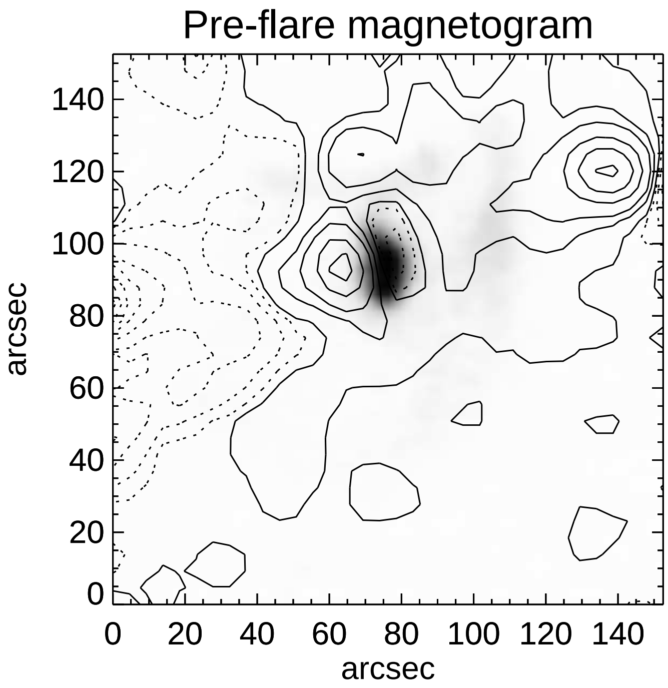

Pre-flare magnetogram
arcsec
arcsec
0
20
40
60
80
100
120
140

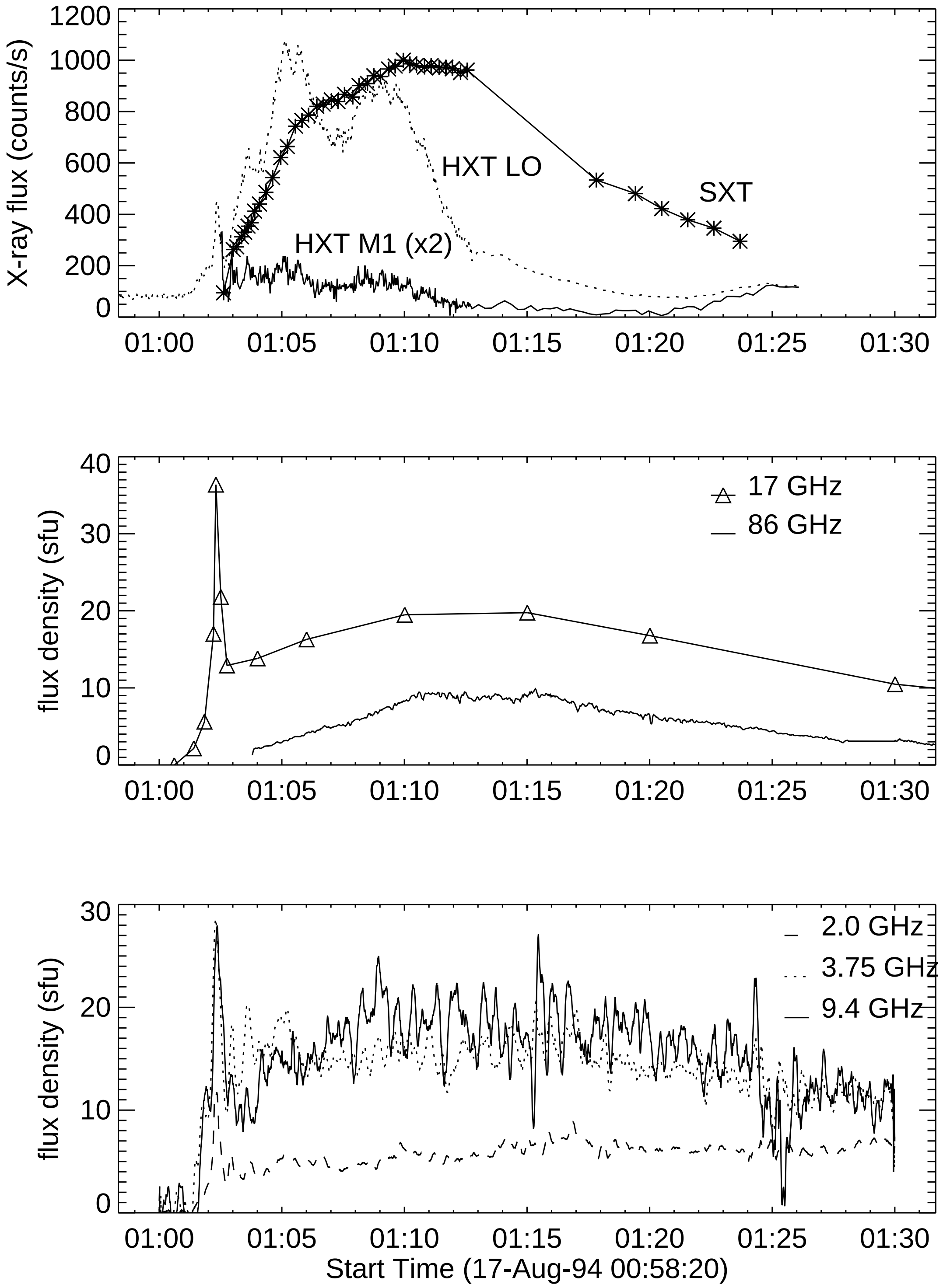
X-ray flux (counts/s)
HXT LO
SXT
HXT M1 (x2)
flux density (sfu)
17 GHz
86 GHz
2.0 GHz
3.75 GHz
9.4 GHz
Start Time (17-Aug-94 00:58:20)

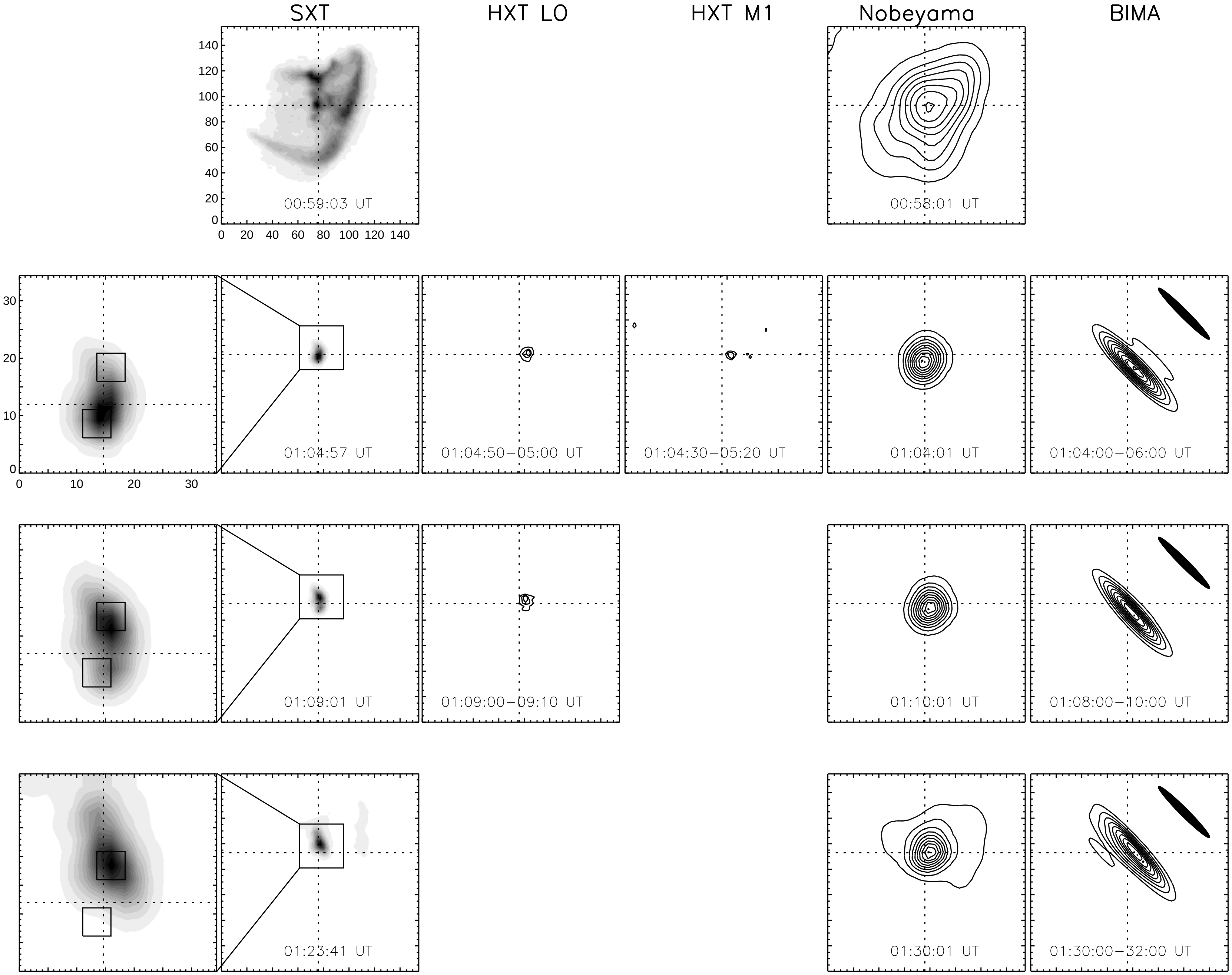
SXT
HXT LO
HXT M1
Nobeyama
BIMA
00:59:03 UT
00:58:01 UT
01:04:57 UT
01:04:50–05:00 UT
01:04:30–05:20 UT
01:04:01 UT
01:04:00–06:00 UT
01:09:01 UT
01:09:00–09:10 UT
01:10:01 UT
01:08:00–10:00 UT
01:23:41 UT
01:30:01 UT
01:30:00–32:00 UT

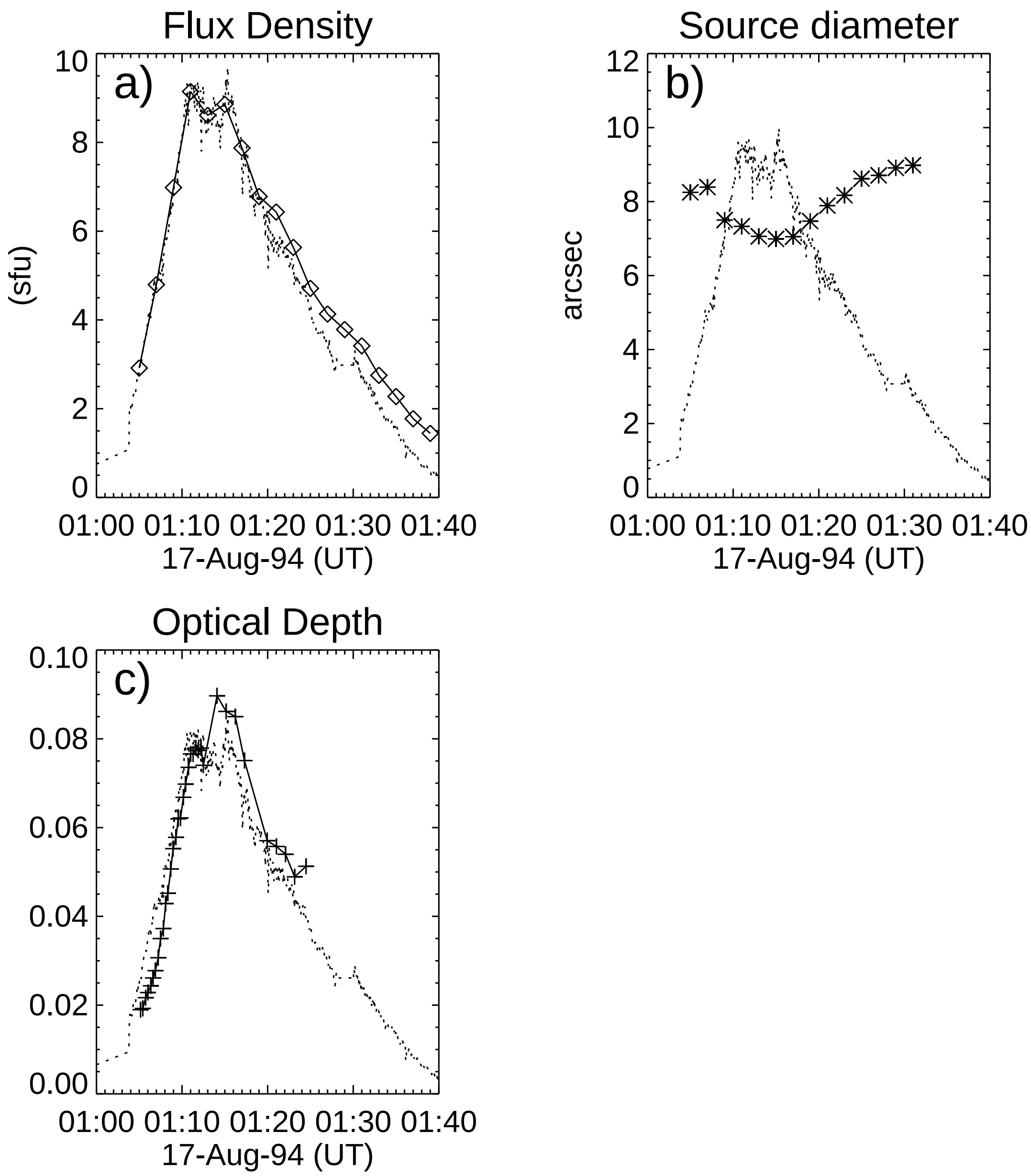

Flux Density
a)
(sfu)
0
2
4
6
8
10
01:00 01:10 01:20 01:30 01:40
17-Aug-94 (UT)
Source diameter
b)
arcsec
0
2
4
6
8
10
12
01:00 01:10 01:20 01:30 01:40
17-Aug-94 (UT)
Optical Depth
c)
0.00
0.02
0.04
0.06
0.08
0.10
01:00 01:10 01:20 01:30 01:40
17-Aug-94 (UT)

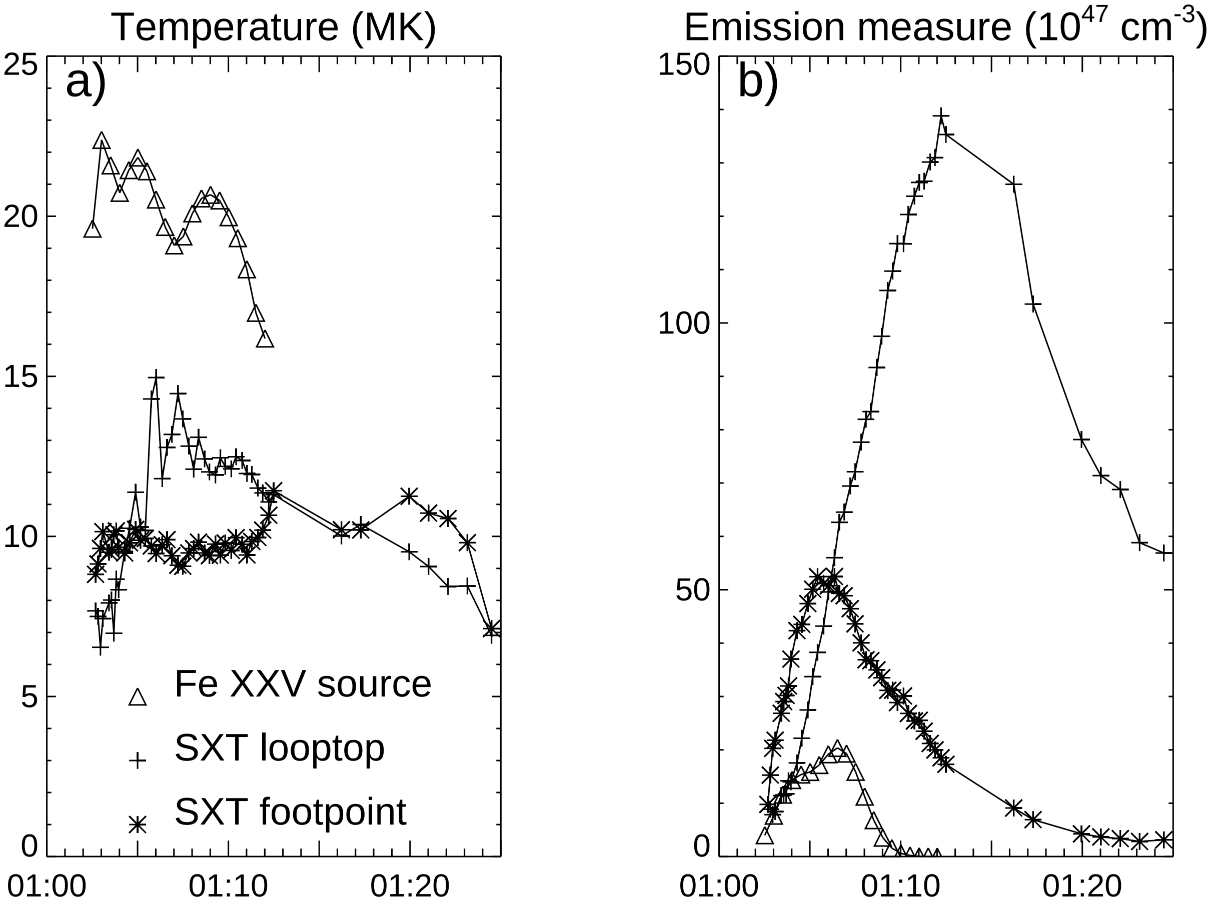

Temperature (MK)
a)
25
20
15
10
5
0
01:00
01:10
01:20
Fe XXV source
SXT looptop
SXT footpoint
Emission measure (10^{47} cm^{-3})
b)
150
100
50
0
01:00
01:10
01:20

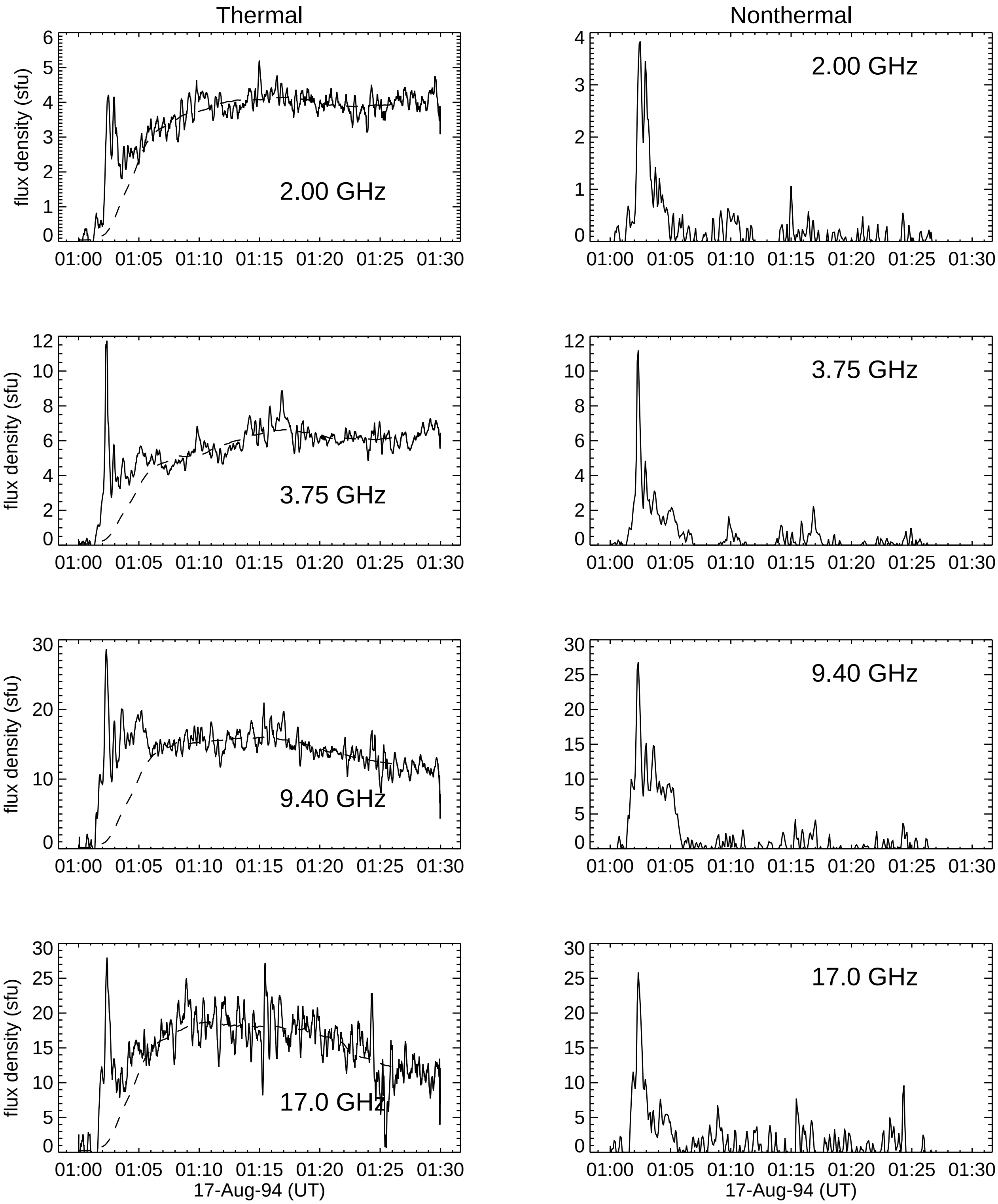

Thermal
Nonthermal
flux density (sfu)
2.00 GHz
3.75 GHz
9.40 GHz
17.0 GHz
01:00
01:05
01:10
01:15
01:20
01:25
01:30
17-Aug-94 (UT)

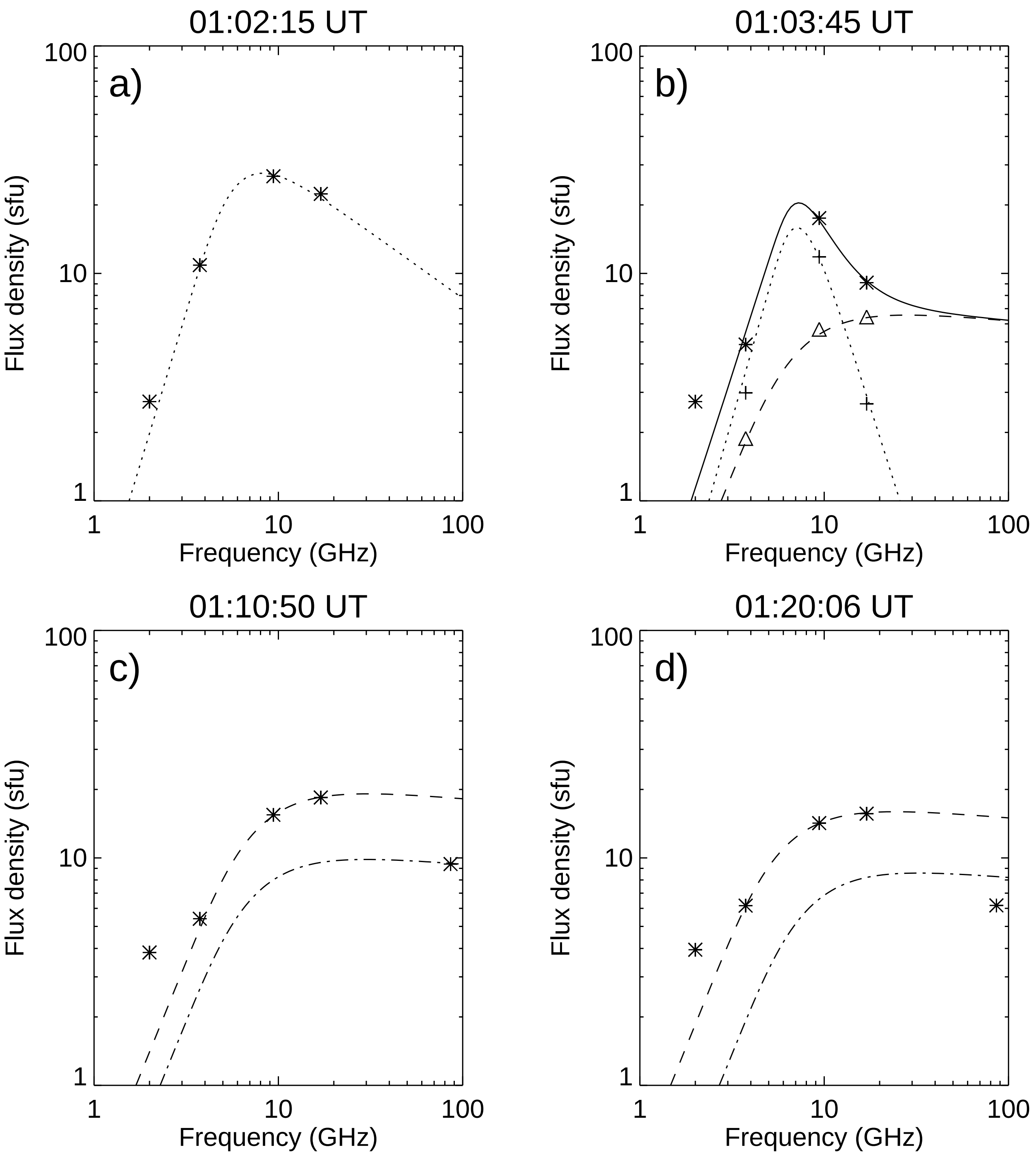
01:02:15 UT
01:03:45 UT
01:10:50 UT
01:20:06 UT
a)
b)
c)
d)
Flux density (sfu)
Frequency (GHz)
1
10
100

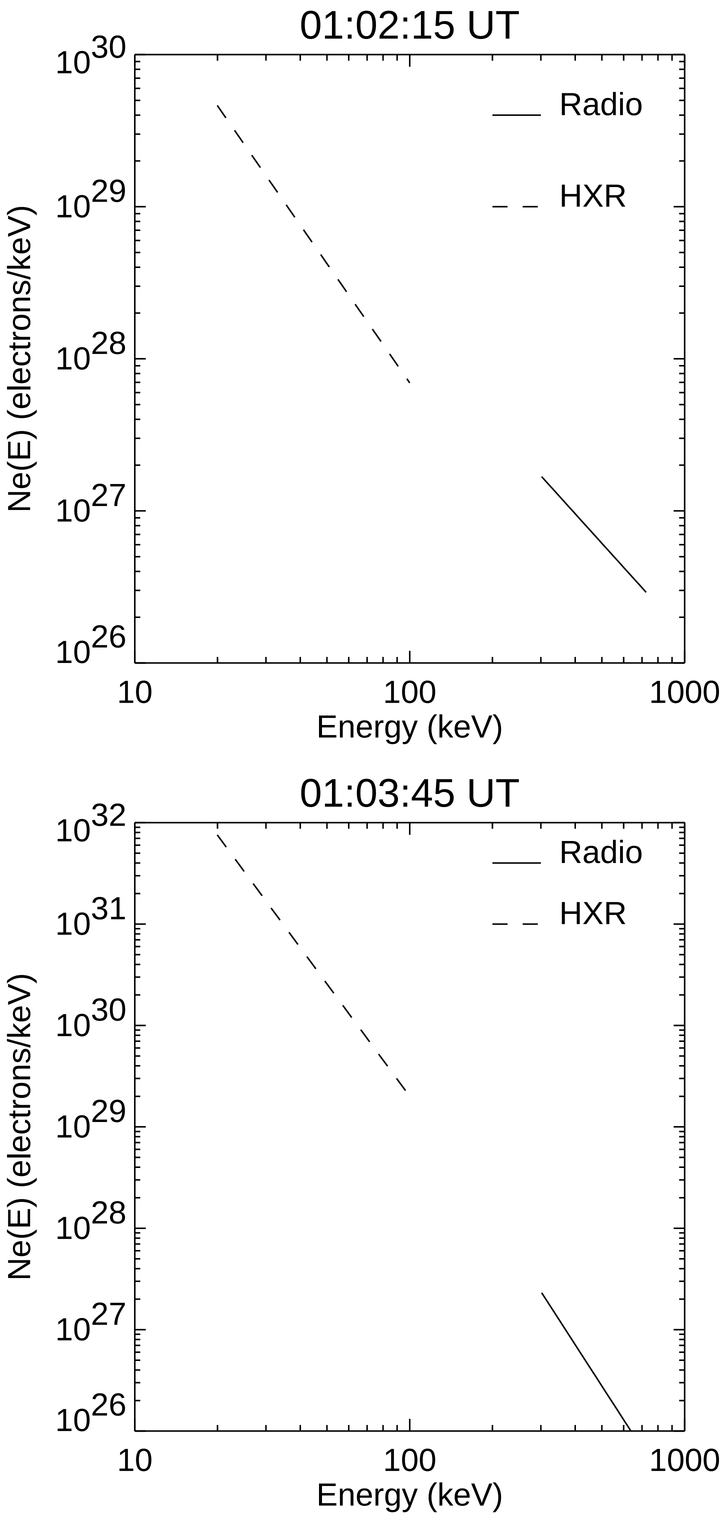
01:02:15 UT
Radio
HXR
Ne(E) (electrons/keV)
10^{30}
10^{29}
10^{28}
10^{27}
10^{26}
10
100
1000
Energy (keV)
01:03:45 UT
Radio
HXR
Ne(E) (electrons/keV)
10^{32}
10^{31}
10^{30}
10^{29}
10^{28}
10^{27}
10^{26}
10
100
1000
Energy (keV)

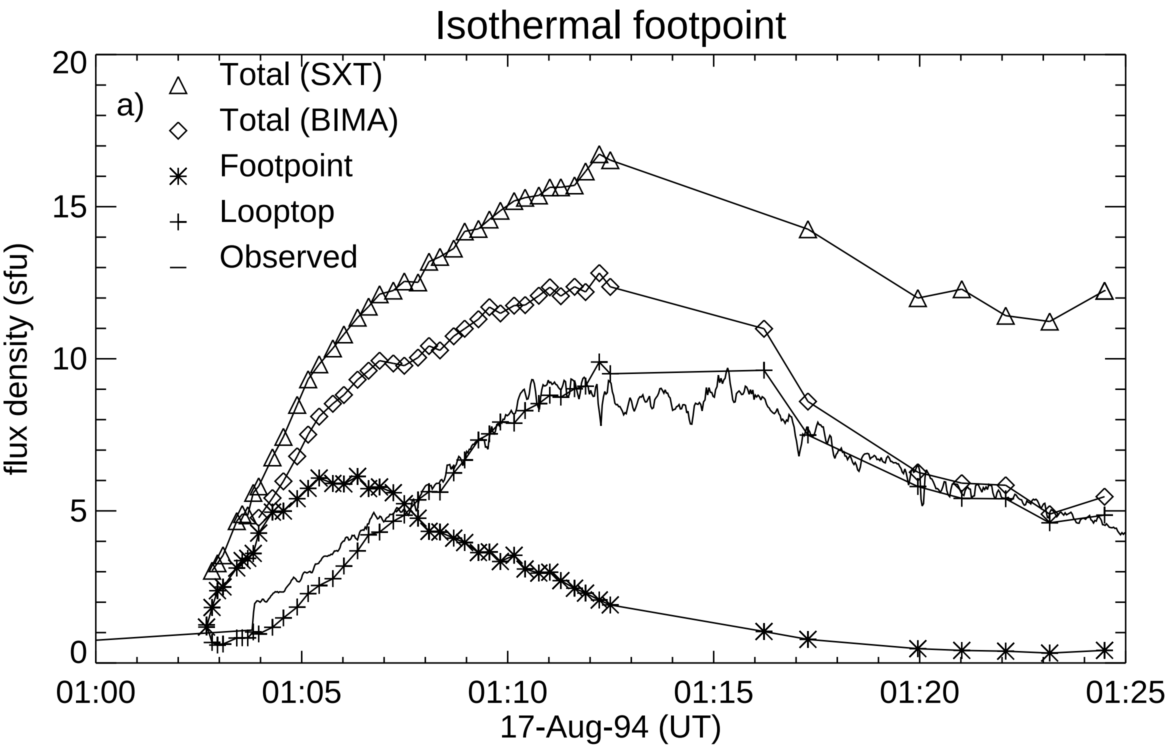
Isothermal footpoint
a)
Total (SXT)
Total (BIMA)
Footpoint
Looptop
Observed
flux density (sfu)
0
5
10
15
20
01:00
01:05
01:10
01:15
01:20
01:25
17-Aug-94 (UT)

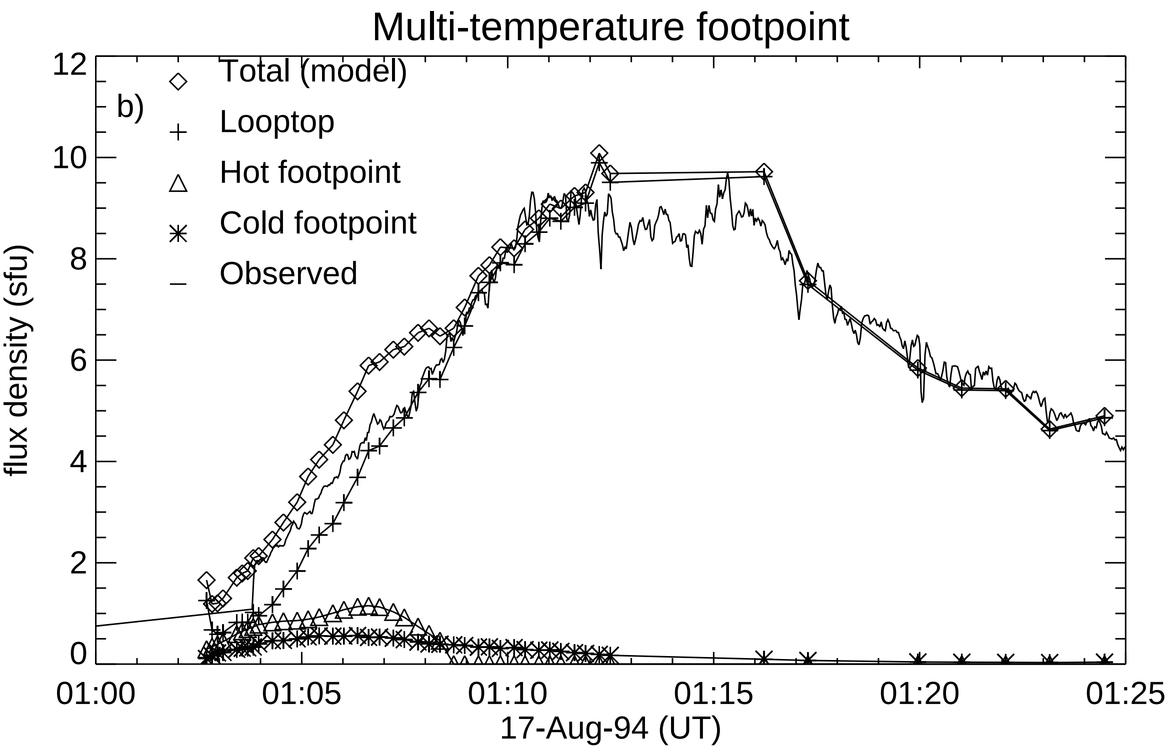
Multi-temperature footpoint
b)
Total (model)
Looptop
Hot footpoint
Cold footpoint
Observed
flux density (sfu)
0
2
4
6
8
10
12
01:00
01:05
01:10
01:15
01:20
01:25
17-Aug-94 (UT)

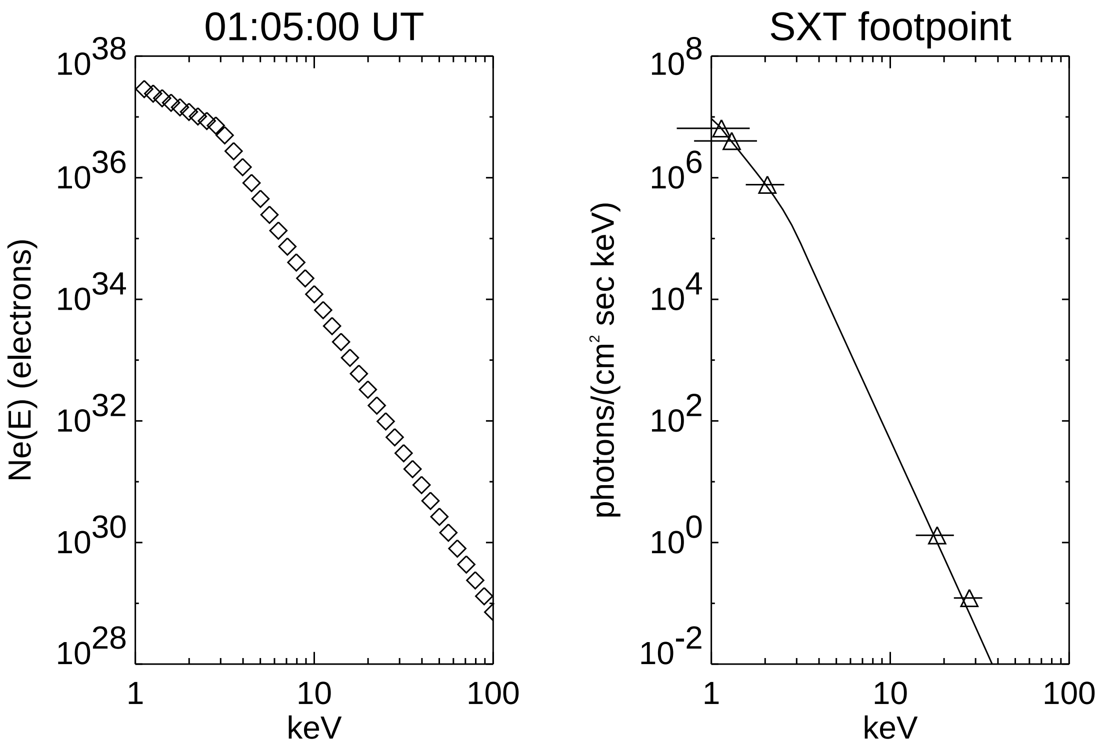

01:05:00 UT
Ne(E) (electrons)
keV
SXT footpoint
photons/(cm² sec keV)
keV